ARTICLE

Journal of Micromechanics and Molecular Physics

A modified phase-field model for predicting mixed-mode fracture in rock-like materials

Zifeng Cheng, Daniel Dias-da-Costa, Yixiang Gan & Luming Shen*

Abstract A phase-field model can continuously smear sharp cracks into diffusive zones with finite width in which the critical energy release rate is commonly determined as constant. However, such an assumption may be insufficient in the case of rock-like materials since the energy release rate can be different for modes I and II cracks. If not accounted for, this could compromise the accuracy of the correct propagation of both wing and secondary cracks. This study proposes an extended, modified phase-field model for simulating a series of Brazilian discs made of a three-dimensional (3D)-printed rock-like material through a time-independent plane strain model. The phase-field model accounts for the splitting of different energy release rates for modes I and II to capture the complex fracture behavior. The novelty of this study lies in not only the theoretical development of the distinction of surface energy release rates but also the qualitative and quantitative assessment of mixed-mode fracture behaviors, which guarantees good predictive capabilities for the location of crack initiation and the direction of crack propagation in various practical applications. Moreover, the modified phase-field model can be implemented easily and fast without introducing new parameters. The numerical results are first validated against experimental data. The impact of the modified energy release rate on crack propagation, particularly on wing cracks, is then numerically investigated. The results show that wing cracks become more dominated by tensile stresses with a decrease in the ratio of modes I and II energy release rates. The phase-field simulations with the modified energy release rate proposed here can reproduce the experimental results both qualitatively and quantitatively with respect to crack propagation patterns, peak loads, crack coalescence loads and coalescence type.

Keywords Phase-field model; mixed-mode fracture; rock-like materials; Brazilian test.

1. Introduction

Pre-existing flaws in a rock mass can result in a catastrophic early failure of significant complexity due to the geometric characteristics of the flaws [1]. The development of numerical models that can predict the behavior requires the handling of crack initiation, propagation, branching and coalescence. Simulating cracking using finite element methods may remain challenging as the discontinuous fields may require special numerical treatment [2], which can be handled by adding extra governing equations and by utilizing other methods to avoid sharp discontinuities in the model [3−5]. The existing numerical methods can be based on discontinuous and continuous approaches. The former group simulates the material separation explicitly by the crack evolution [5−7]. This group originates from the early remeshing methods [8] in which the crack propagates along the element boundary. In contrast, the development of the extended finite element method (XFEM) and the cohesive zone method could overcome this problem by using enrichment techniques [3, 7], which allows the simulation of crack propagation, coalescence, branching and nucleation. On the other hand, a sharp crack can be represented by a smeared zone of degraded solid with a finite width by using continuous approaches such as phase-field method [4, 9].

The phase-field method has been attracting great interest in the last 10 years [10−12]. The key feature of this method is that the crack is represented by a phase-field variable, which varies between 0 and 1. The diffusion of a sharp crack is achieved by using an exponential function where a length parameter controls the width of the smeared crack path [10, 11]. The initial development of the phase-field method was based on the variational approach proposed by Francfort and Marigo [13], which can be regarded as an improvement from the classical Griffith's theory [14, 15]. In the phase-field method, the creation of a new crack surface is described by the relation between the strain energy stored in the material and the surface energy [10−13]. The phase-field method is relatively easy to implement and can predict cracking even in the presence of a complex topology [4, 10−13, 16]. Due to its inherent advantages, the phase-field method has been further extended for dynamic fracture [17], fracture of elastic-plastic materials [18], and hydraulic fracture [19].

One main characteristic of brittle rock-like materials is that their tensile strength is significantly lower than their compressive strength, and the investigation of fracture behavior of the tension-sensitive rock-like materials includes not only the position of crack initiation but also the accurate propagation paths [14, 17, 20−22]. For pre-flawed rock mass and rock-like materials, it can be

School of Civil Engineering, The University of Sydney, NSW 2006, Australia
*luming.shen@sydney.edu.au
*Corresponding author.

Received 30 June 2022; Revised 15 August 2022; Accepted 31 August 2022; Published 30 September 2022; doi:10.1142/S2424913022410065

observed in many studies that both primary wing cracks and secondary shear cracks generally initiate at flaw tips, which are impacted by the flaw inclination and the material type [24]. In addition, the crack coalescence of rock specimens with double or multiple flaws are always of great importance to be characterised for revealing fracture behaviors of natural rocks Brazilian discs with or without pre-existing flaws, have been widely adopted as one of the standard tests for assessing the fracture behavior of rocks and rock-like materials, including the determination of the tensile strength [23−27]. Various numerical methods, such as the discrete element method (DEM), were used to support the analysis and interpretation of data on those tests [30, 39]. The energy release rate in the phase-field method was usually assumed as a constant to control both modes I and II cracks simultaneously [28, 29, 33]. However, it is worth noting that the energy release rate g_c of rock-like materials for mode I fracture is usually much smaller than that for mode II cracks, and their ratio varies for different materials [31, 32]. The observed results of Brazilian tests were very different for different rock-like materials with different energy release rate ratios, even though the geometric characteristics of the discs were similar [32]. The considerable difference between these experimental observations may result from the intrinsic properties of the materials, which indicates the importance of the energy release rate ratio for different materials. Zhang *et al.* [31] proposed a modification scenario for the distinction of energy release rates for the phase-field approach and tested the model with a single-flawed square plate and double-flawed rectangular plates. Another phase-field model with consistent kinematic modes for anisotropic rocks was proposed by Bryant and Sun [40], which was based on modified *G*-criterion. In their study, a search algorithm for crack direction was introduced for dealing with the local energy dissipation maximization problem. In addition, Wang *et al.* [41] proposed a phase-field model with a unified tensile fracture criterion [41], where the ratio of the critical shear stress to critical tensile stress was introduced for linking the two energy release rates for modes I and II.

This study aims to develop a modified quasi-static phase-field model to numerically investigate the effect of energy release rate on the fracture behaviors of the pre-flawed Brazilian discs made from rock-like three-dimensional (3D)-printed materials. The simulation cases are based on the experiments conducted by Sharafisafa *et al.* [24], which include tests on discs with single- and double-inclined flaws. The impact of the energy release rates for modes I and II cracks on both the pattern of wing cracks and the development of secondary shear cracks is investigated. Moreover, the fracture mechanism and, in particular, the coalescence of inner cracks in rock bridge zone in the double-flawed Brazilian tests is studied.

The remaining sections of the paper are given as follows. The foundation of the phase-field model is introduced in Sec. 2, which is followed by the details of the finite element implementation of the proposed model, as well as the modification of the energy release rate ratio in Sec. 3. The numerical simulation setup is presented in Sec. 4. In Sec. 5, the experimental results for Brazilian tests are reproduced by the proposed model. Five examples containing single- and double-inclined flaws are simulated. The comparison of the crack initiation, propagation and coalescence between the experimental and the numerical results is given. The concluding remarks are given in the final section.

2. Phase-Field Model for Brittle Fracture

The main feature of the phase-field model is that the state of the crack is represented by the smooth transition of a scalar variable φ called the phase-field. As introduced by Miehe *et al.* [10], an exponential function is used as a typical approximation of a non-smooth crack, of which the one-dimensional (1D) illustration is shown in Fig. 1. Here, l_c is the characteristic length parameter which dominates the width of the diffusive zone.

Consider an arbitrary 3D solid body $\Omega \subset \mathbb{R}^d$ $(d \in \{1, 2, 3\})$ with a crack surface Γ, as shown in Fig. 2(a), where the intact part is represented by a phase-field variable $\varphi = 0$ while $\varphi = 1$ indicates a sharp crack. The external boundary $\partial\Omega$ is composed of the Dirichlet boundary $\partial\Omega_u$ and the Neumann boundary $\partial\Omega_t$. The diffusion of the sharp discontinuities by the phase-field is illustrated in Fig. 2(b).

Based on the classical Griffith's theory, the total energy includes the strain energy stored in the undamaged solid and the surface energy required for creating the crack surface [14]. A variational approach proposed by Francfort *et al.* [12] improves the original Griffith's theory into the problem of energy minimization. A brief description of this variational principle is given below, and more details of the derivation can be found in Refs. 12 and 13. The

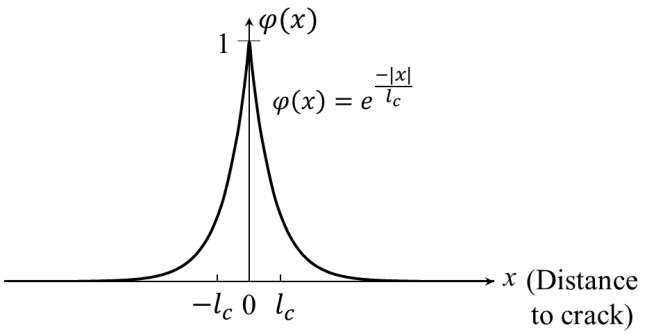

Fig. 1. 1D smeared crack topology.

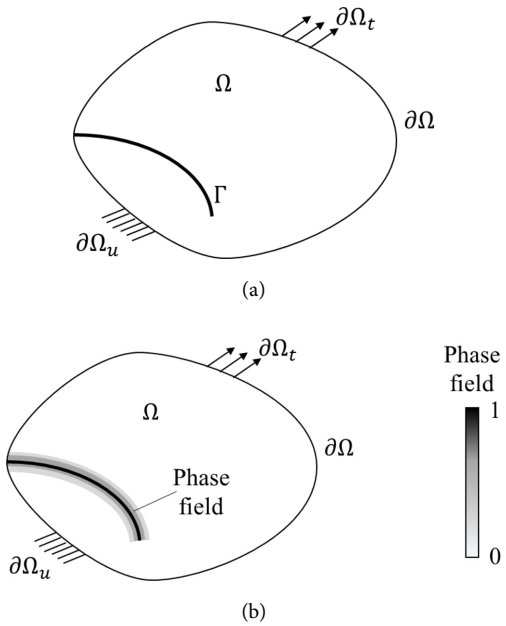

Fig. 2. Schematic illustration of a solid body with (a) a sharp crack Γ; (b) a smeared crack represented by the phase-field for approximating sharp discontinuities.

functional of the total energy is given by

$$W(\Gamma,\boldsymbol{u}) = \int_{\Omega}\psi(\boldsymbol{u},\varphi)d\Omega + \int_{\Gamma} g_c d\Gamma - \int_{\Omega}\boldsymbol{b}\cdot\boldsymbol{u}d\Omega - \int_{\partial\Omega_t}\boldsymbol{t}\cdot\boldsymbol{u}d\mathrm{S}. \tag{2.1}$$

The first two components at the right-hand side of the previous equation are the strain energy and surface energy, respectively, while the other two negative components represent the work done by the body force and traction on the boundary. Here, $\boldsymbol{u}$, ψ, g_c, $\boldsymbol{b}$ and $\boldsymbol{t}$ are displacement, elastic energy density, energy release rate, body force and traction on the boundary, respectively. In addition, $\int_\Gamma d\Gamma$ is the crack surface density. Based on the work by Miehe *et al.* [11], the crack functional can be approximated as:

$$\int_{\Gamma} d\Gamma = \int_{\Omega}\gamma(\varphi,\nabla\varphi)d\Omega, \tag{2.2}$$

in which $\gamma(\varphi,\nabla\varphi)$ is the crack surface density given by

$$\gamma(\varphi,\nabla\varphi) = \int_{\Omega}\left\{\frac{1}{2l_c}\varphi^2 + \frac{l_c}{2}|\nabla\varphi|^2\right\}d\Omega. \tag{2.3}$$

Accordingly, the surface energy function can be rewritten as

$$\int_{\Gamma} g_c d\Gamma = \int_{\Omega} g_c * \left\{\frac{1}{2l_c}\varphi^2 + \frac{l_c}{2}|\nabla\varphi|^2\right\}dV. \tag{2.4}$$

The elastic energy density ψ_0 for the intact elastic solid is directly dependent on elastic strain, which can be given by [10]:

$$\psi_0(\boldsymbol{\varepsilon}(\boldsymbol{u})) = \frac{1}{2}\boldsymbol{\varepsilon}^T C_0\boldsymbol{\varepsilon} = \frac{\lambda\langle tr(\boldsymbol{\varepsilon})\rangle^2}{2} + \mu tr(\boldsymbol{\varepsilon}^2), \tag{2.5}$$

where C_0, λ and μ are the linear elastic stiffness matrix, elastic bulk modulus and shear modulus, respectively. The stress tensor is calculated as

$$\boldsymbol{\sigma} = g(\varphi)C_0\boldsymbol{\varepsilon}, \tag{2.6}$$

where the degradation function $g(\varphi)$ is commonly chosen as [11, 34]:

$$g(\varphi) = (1-\varphi)^2. \tag{2.7}$$

Since the phase-field directly indicates the crack as well as the solid degradation, the elastic energy density of the damaged solids is given by

$$\psi(\boldsymbol{u},\varphi) = g(\varphi)\psi_0(\boldsymbol{\varepsilon}(\boldsymbol{u})). \tag{2.8}$$

In Eq. (2.8), the degradation can be caused by both tension and compression. As a result, the crack initiation may be triggered by compressive strain, which may not be realistic [11, 30]. In addition, cracks can be reversible if the energy degradation in tension and compression is not separated [11, 31, 34]. Accordingly, the previous equation can be further expanded by splitting the strain tensor into positive and negative parts as follows:

$$\psi_0(\boldsymbol{\varepsilon}) = \psi_0^+(\boldsymbol{\varepsilon}_+) + \psi_0^-(\boldsymbol{\varepsilon}_-), \tag{2.9}$$

where the energy degradation is controlled by the tensile strain, which is further given by

$$\psi(\boldsymbol{\varepsilon},\varphi) = (1-\varphi)^2 * \psi_0^+(\boldsymbol{\varepsilon}_+) + \psi_0^-(\boldsymbol{\varepsilon}_-). \tag{2.10}$$

More details of the strain decomposition can be found in Refs. 10, 11 and 34.

Finally, the total energy functional shown in Eq. (2.1) can be rewritten as

$$W(\Gamma,\boldsymbol{u}) = \int_{\Omega}[(1-\varphi)^2 * \psi_0^+(\boldsymbol{\varepsilon}_+) + \psi_0^-(\boldsymbol{\varepsilon}_-)]d\Omega + \int_{\Omega} g_c * \left\{\frac{1}{2l_c}\varphi^2 + \frac{l_c}{2}|\nabla\varphi|^2\right\}dV - \int_{\Omega}\boldsymbol{b}\cdot\boldsymbol{u}d\Omega - \int_{\partial\Omega_t}\boldsymbol{t}\cdot\boldsymbol{u}d\mathrm{S}. \tag{2.11}$$

With the description of the phase-field approximation for the fracture energy at hand, the governing equations can be determined next. Since the key feature of the variational approach is to calculate the crack by minimizing the energy functional [12, 13], the first-order variation of the total energy functional δW should be zero. Accordingly, the equations in the strong form are written as

$$\nabla\cdot\boldsymbol{\sigma} + \boldsymbol{b} = \boldsymbol{0} \text{ in } \Omega, \tag{2.12}$$

$$\boldsymbol{\sigma}\cdot\boldsymbol{n} = \boldsymbol{t} \text{ on } \partial\Omega_t \tag{2.13}$$

Along with the Dirichlet boundary condition

$$\boldsymbol{u} = \bar{\boldsymbol{u}} \text{ on } \partial\Omega_u, \tag{2.14}$$

where $\boldsymbol{n}$ is the normal vector pointing outward of the boundary.

As for the phase-field

$$\nabla\varphi\cdot\boldsymbol{n} = 0 \text{ on } \partial\Omega. \tag{2.15}$$

To prevent crack recovery, the elastic energy density in Eq. (2.8) is substituted by a history field H. According to Miehe *et al.* [11], H describes the maximum reference energy attained, which is

$$\mathrm{H} = \max\psi_0^+(\boldsymbol{\varepsilon}_+), \tag{2.16}$$

and the strong form of the phase-field problem can be written as

$$2(1-\varphi)\mathrm{H} - \frac{g_c}{l_c}\varphi + g_c l_c\Delta\varphi = 0. \tag{2.17}$$

Therefore, the governing equations of the phase-field method are summarised as follows:

$$\begin{cases} \nabla\cdot\boldsymbol{\sigma} + \boldsymbol{b} = 0 \text{ in } \Omega, \\ \boldsymbol{\sigma}\cdot\boldsymbol{n} = \boldsymbol{t} \text{ on } \partial\Omega_t, \\ 2(1-\varphi)\mathrm{H} - \dfrac{g_c}{l_c}\varphi + g_c l_c\Delta\varphi = 0, \\ \boldsymbol{u} = \bar{\boldsymbol{u}} \text{ on } \partial\Omega_u, \\ \boldsymbol{\nabla}\varphi\cdot\boldsymbol{n} = 0 \text{ on } \partial\Omega. \end{cases} \tag{2.18}$$

3. Numerical Implementation and Modification

In this study, the phase-field method is implemented by using the finite element approach to discretise the solid domain. All the functionals mentioned in the previous section are dependent on the vector displacement field $\boldsymbol{u}$ and the scalar phase-field φ. The discretization using nodal variables is given by

$$\boldsymbol{u} = \sum_i^n N_u\boldsymbol{u}_i, \tag{3.1}$$

$$\varphi = \sum_i^n N_\varphi\varphi_i. \tag{3.2}$$

For a brittle solid domain discretised with n nodes, N_u and N_φ are the shape functions of displacement $\boldsymbol{u}$ and phase-field φ, respectively,

while $\boldsymbol{u}_i$ and φ_i represent the nodal values. Their derivatives can be written as

$$\boldsymbol{\varepsilon} = \nabla \boldsymbol{u} = \sum_i^n \boldsymbol{B}_u \boldsymbol{u}_i, \tag{3.3}$$

$$\nabla \varphi = \sum_i^n \boldsymbol{B}_\varphi \varphi_i, \tag{3.4}$$

where $\boldsymbol{B}_u$ and $\boldsymbol{B}_\varphi$ are the derivatives of N_u and N_φ, respectively.

The weak form of the phase-field modeling is expressed by

$$\begin{aligned} \boldsymbol{r}^u &= \boldsymbol{F}^{u,\text{ext}} - \boldsymbol{F}^{u,\text{int}} \\ &= \int_\Omega \boldsymbol{B}_{\boldsymbol{u}}^T \sigma d\Omega - \int_\Omega \boldsymbol{N}_u^T \boldsymbol{b} d\Omega + \int_{\partial\Omega_t} \boldsymbol{N}_{\boldsymbol{u}}^T \cdot \boldsymbol{t} d\mathrm{S}, \end{aligned} \tag{3.5}$$

$$\boldsymbol{r}^\phi = \int_\Omega \left\{ \left[\frac{g_c}{l_c}\varphi - 2(1-\varphi)H \right] \boldsymbol{N}_\phi^T + g_c l_c \boldsymbol{B}_\phi^T \nabla \phi \right\} d\Omega, \tag{3.6}$$

where $\boldsymbol{r}^u$ and $\boldsymbol{r}^\phi$ are the residual vectors of displacement and phase-field, and $\boldsymbol{F}^{u,\text{ext}}$ and $\boldsymbol{F}^{u,\text{int}}$ are the external and the internal forces, respectively. As proposed by Molnár and Gravouil [34], a staggered algorithm is used here for calculating the displacement and phase-field separately. At each time step, the displacement field is updated first by freezing the phase-field, which is followed by updating the phase-field using the updated displacement. Accordingly, the fracture problem can be iteratively solved with the Newton–Raphson method [34], which is written as

$$\begin{Bmatrix} \phi \\ \boldsymbol{u} \end{Bmatrix}_{n+1} = \begin{Bmatrix} \phi \\ \boldsymbol{u} \end{Bmatrix}_n - \begin{bmatrix} \boldsymbol{K}^{\phi\phi} & 0 \\ 0 & \boldsymbol{K}^{uu} \end{bmatrix} \begin{Bmatrix} \boldsymbol{r}^\phi \\ \boldsymbol{r}^u \end{Bmatrix}_n, \tag{3.7}$$

where the tangent stiffness matrices are calculated as [30, 34, 38]

$$\boldsymbol{K}^{\phi\phi} = \int_\Omega \left[g_c l_c \boldsymbol{B}_\phi^T \nabla \phi + \left(\frac{g_c}{l_c} + 2\mathrm{H} \right) \boldsymbol{N}_\phi^T \boldsymbol{N}_\phi \right] d\Omega, \tag{3.8}$$

$$\boldsymbol{K}^{uu} = \int_\Omega [g(\varphi) \boldsymbol{B}_{\boldsymbol{u}}^T \boldsymbol{C}_0 \boldsymbol{B}_{\boldsymbol{u}}] d\Omega. \tag{3.9}$$

To solve the minimization problem indicated by Molnár and Gravouil [34], the phase-field is determined as

$$\varphi = \frac{\frac{2\mathrm{H}}{g_c}}{\frac{1}{l_c} + \frac{2\mathrm{H}}{g_c}}. \tag{3.10}$$

Notably, the difference of the energy release rates of rock-like materials for modes I and II cracks cannot be neglected. Indeed, $g_{c,I}$ for mode I cracks is usually significantly smaller than $g_{c,II}$ for mode II cracks [31, 32]. Therefore, the utilization of a single constant for g_c is unrealistic and will not be acceptable in most cases. As proposed by Zhang *et al.* [31], the two components of the elastic energy in Eq. (2.7) correspond to mode I and mode II cracks, respectively. Hence, two energy release rates should be assigned to these two components separately to distinguish the different failure modes. Accordingly, the history field is modified as follows:

$$H_I = \max\left(\frac{\lambda \langle tr(\boldsymbol{\varepsilon}) \rangle_+^2}{2} \right), \tag{3.11}$$

$$H_{II} = \max(\mu tr(\boldsymbol{\varepsilon}_+^2)). \tag{3.12}$$

Then the governing equation (2.18) becomes

$$2(1-\varphi)\left(\frac{H_I}{g_{c,I}} + \frac{H_{II}}{g_{c,II}} \right) - \frac{1}{l_c}\varphi + l_c \Delta \varphi = 0. \tag{3.13}$$

For the minimization problem, the phase-field in Eq. (3.10) is correspondingly rewritten as

$$\varphi = \frac{2\left(\frac{H_I}{g_{c,I}} + \frac{H_{II}}{g_{c,II}} \right)}{\frac{1}{l_c} + 2\left(\frac{H_I}{g_{c,I}} + \frac{H_{II}}{g_{c,II}} \right)}. \tag{3.14}$$

4. Numerical Simulation Setup

Based on the equations provided in the previous section, a two-dimensional (2D) time-independent phase-field model is implemented for simulating the brittle fracture of a series of single- and double-flawed Brazilian discs. The numerical simulation is carried out after the implementation of the user-defined element (UEL) and user-defined material (UMAT) routines in ABAQUS 2018 [42].

The proposed model is validated by the experiments conducted by Sharafisafa *et al.* [24] in which the crack propagation and coalescence in the rock-like pre-flawed Brazilian discs were investigated. The schematic of the specimen geometry is illustrated in Fig. 3. The diameter and the thickness of the discs are 40 and 15 mm, respectively. The pre-existing flaw is 8 mm long and 0.6 mm wide. The 3D-printed discs are made of calcium sulphate hemihydrate $CaSO_4\frac{1}{2}H_2O$. It is worth noting that the range of Young's modulus of this 3D-printed material can vary from less than 100 MPa to over 1 GPa, which may depend on printing orientations, nozzle pattern of the printed head, powder supply method, printing speed and so on [24, 35, 36]. In addition, the stress–strain curves from experiments are usually non-linear and a secant modulus is commonly chosen for calculating the material's Young's modulus [24, 35]. Accordingly,

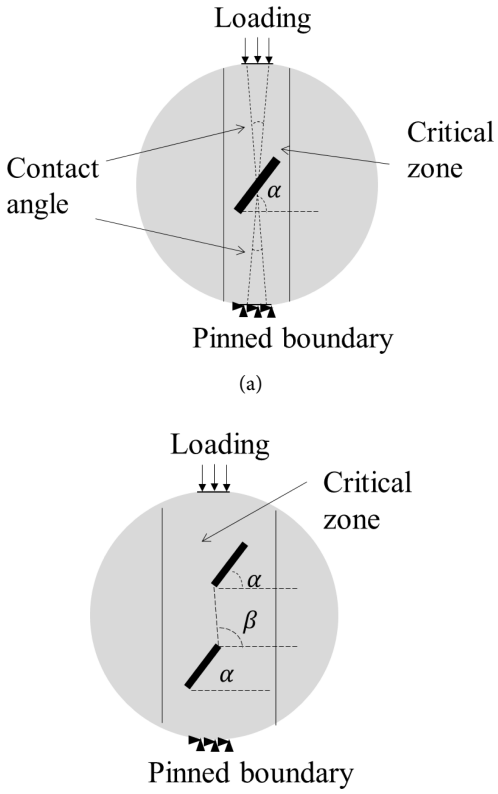

Fig. 3. Schematic illustration of the numerical setup of (a) a single-flawed Brazilian test; (b) a double-flawed Brazilian test.

the selection of the secant line on the stress−strain curve can also influence the calculation of Young's modulus. Young's modulus and Poisson's ratio for the simulations here are chosen to be 400 and 0.285 MPa, respectively. In addition, the tensile strength of 1.85 MPa and the plane strain toughness of $0.47\text{m}^{0.5} \cdot \text{MPam}^{0.5}$ are adopted. A 2D finite element model with the proposed phase-field model is established to simulate the single- and double-flawed Brazilian discs under compression. The element type of CPS4R is adopted.

As mentioned above, one characteristic of the phase-field model is that the sharp crack is diffused to a 2D zone with finite width, which is dependent on the length parameter and mesh size. Therefore, the mesh size of the cracked part (the "critical zone" illustrated in Fig. 3) should be fine enough to obtain relatively accurate results. Note the size of the critical zone with a finer mesh is dependent on the orientation of the inclined flaw to include the potential crack paths. The mesh sizes of the critical and non-critical zones are set to be 0.1 and 1 mm, respectively, after a first convergence study. According to Miehe *et al.* [11], the ratio of the length parameter and mesh size should be sufficiently small to capture accurate crack paths but should not be less than two times the mesh size to achieve an accurate crack topology approximation. Therefore, the length parameter is determined to be $l_c = 0.2$ mm. Unlike the experiments where the discs are compressed by directly contacting with steel plates, the flattened boundaries are directly applied to the top and bottom surfaces of all models, and the top load is distributed along the horizontal chord. The contact angle between the steel bar and the disc usually ranges between 10° and 20° in several previous experiments depending on Young's modulus of the material [24−27, 37]. Therefore, the contact angle for the simulation is chosen to be 15° and the corresponding length of flattened loading arcs is 5.2 mm. The compressive load is simulated by increasing the vertical displacement on the top surface with the bottom boundary pinned in both x- and y-directions. Following the experiments, the total vertical displacement is set to be 1 mm and the displacement increment is $\Delta u = 1 \times 10^{-3}$ mm.

5. Simulation Results and Discussion

5.1. Brazilian discs with single flaw

A series of single-flawed Brazilian discs under quasi-static compressive load is simulated first. The first disc has a single 45° inclined flaw. The width of the critical zone is set to be 11 mm to include the potential crack paths, and a total of 55,000 quadrilateral elements (4-nodes bi-linear type CPS4R) are used in this model. This test is firstly simulated using the standard phase-field model as a benchmark, where $g_{c,I} = g_{c,II} = 0.1$ N/mm. The convergence study on mesh size is shown in Fig. 4, which leads to the selection of a size of 0.1 mm with the ratio of mesh size to l_c being 0.5. The crack evolution process is illustrated in Fig. 5. Two symmetric cracks initiate at each tip of the pre-existing flaw, where the value of the phase-field reaches 1.0 first. With increasing tensile and shear strains, the crack propagation is first almost perpendicular to the pre-existing flaw, then gradually changes to the vertical direction and finally reaches the top and bottom of the disc.

The curved crack pattern results from the effect of the mixed-mode fracture. However, the experimental results confirm that most parts of the crack paths are nearly vertical, hence dominated by mode I [24]. Therefore, the model should account for the difference in energy release rates for modes I and II cracks. Two additional values of the energy release rate ratio $\frac{g_{c,I}}{g_{c,II}}$ of 0.5 and 0.1, are considered in the simulations. The final crack patterns of these two

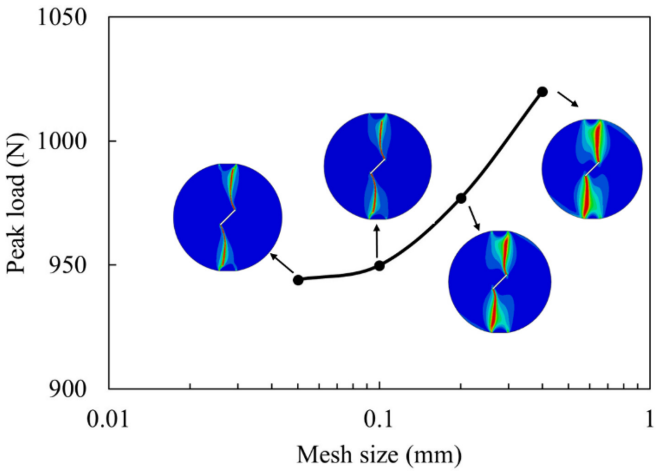

Fig. 4. Convergence study on mesh size (with the ratio of mesh size to l_c being 0.5).

simulations and the one with $\frac{g_{c,I}}{g_{c,II}} = 1$ are shown in Figs. 6(a)−6(c), while Figs. 6(d) and 6(e) are the simulated ε_{xx} contour for direct comparison with the experimental result in Fig. 6(g). It can be seen from the figures that the initial crack propagation is nearly identical in all cases. However, the crack path with a smaller energy release rate ratio tends to be vertical earlier than that with a larger ratio, which is expected. Based on the comparison between the final crack patterns and the strain contour from the experiment (shown in Fig. 6(g)), the energy release rate ratio of $\frac{g_{c,I}}{g_{c,II}} = 0.1$ is chosen to depict the fracture behavior of this type of 3D-printed material. To better compare the results, the crack patterns from three simulations are represented in Fig. 6(h), where the origin is the point of crack initiation point at the tip of the bottom flaw.

As presented in Fig. 6, the simulated fracture pattern with $\frac{g_{c,I}}{g_{c,II}} = 0.1$ matches the experimental result better for the single-flawed disc with $\alpha = 45°$. Firstly, only two wing cracks initiate at the flaw tips and propagate until the ultimate failure takes place, and there are no secondary cracks in either the experiment or the simulations. Based on the crack opening displacement and the failure pattern contour from the experiment [24], not only the crack initiation but also the propagation of crack at failure from the model with $\frac{g_{c,I}}{g_{c,II}} = 0.1$ are consistent with the experimental observation. More importantly, the end point of crack from the model with $\frac{g_{c,I}}{g_{c,II}} = 0.1$ locates at the boundary right below the flaw tip, which is in good agreement with the experiments. The occurrence of the secondary cracks in pre-flawed tests is deemed to be dependent on the material properties and the topological characteristics of the specimen. There are no other diagonal shear zones being observed in the phase-field contour to trigger the propagation of the secondary shear cracks, which is consistent with the experiment as well. As for the propagation path of the two primary wing cracks, the energy release rates for modes I and II have a considerable impact on the propagation path. With the decrease of $g_{c,I}$, the degradation of corresponding elements at the crack tips is more influenced by the normal strain than the shear strain. As a result, the crack path in the modified model becomes almost vertical towards the loading points at an earlier stage, while that in the unmodified model is more curvilinear. On the other hand, the modified $g_{c,I}$ and $g_{c,II}$ have little impact on the crack initiation: the orientation of the initial crack at the two tips from Figs. 6(a)−6(c) are almost identical. Referring to Eqs. (2.11) and (2.17), the crack evolution is dominated by the relations

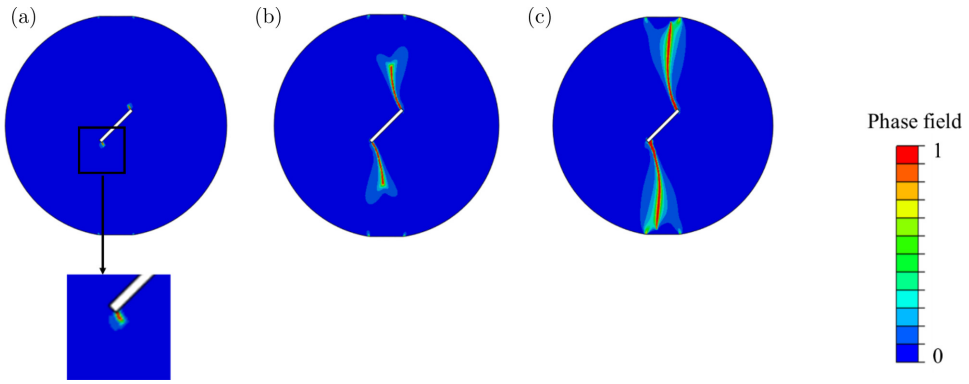

Fig. 5. Crack evolution for a Brazilian disc with a 45° inclined single flaw for the displacement at (a) $u = 0.49$ mm; (b) $u = 0.72$ mm; (c) $u = 0.81$ mm from the unmodified phase-field model with $g_{c,I} = g_{c,II} = 0.1$ N/mm.

between energy history (related to maximum strain energy) and surface energy, where the relationship is reflected by the ratio $\frac{H}{g_c}$. Therefore, whether the crack is dominated by tension or shear can be quantitively visualised by comparing the ratio $\frac{H}{g_c}$ for modes I and II.

To further investigate the mechanism of crack initiation, the simulated maximum principal stress, and maximum shear stress, as well as the ratio $\frac{H}{g_c}$, for modes I and II at the crack initiation stage, are given in Fig. 7. From the magnified image of the tip of the bottom flaw, the maximum value of the maximum principal stress is located

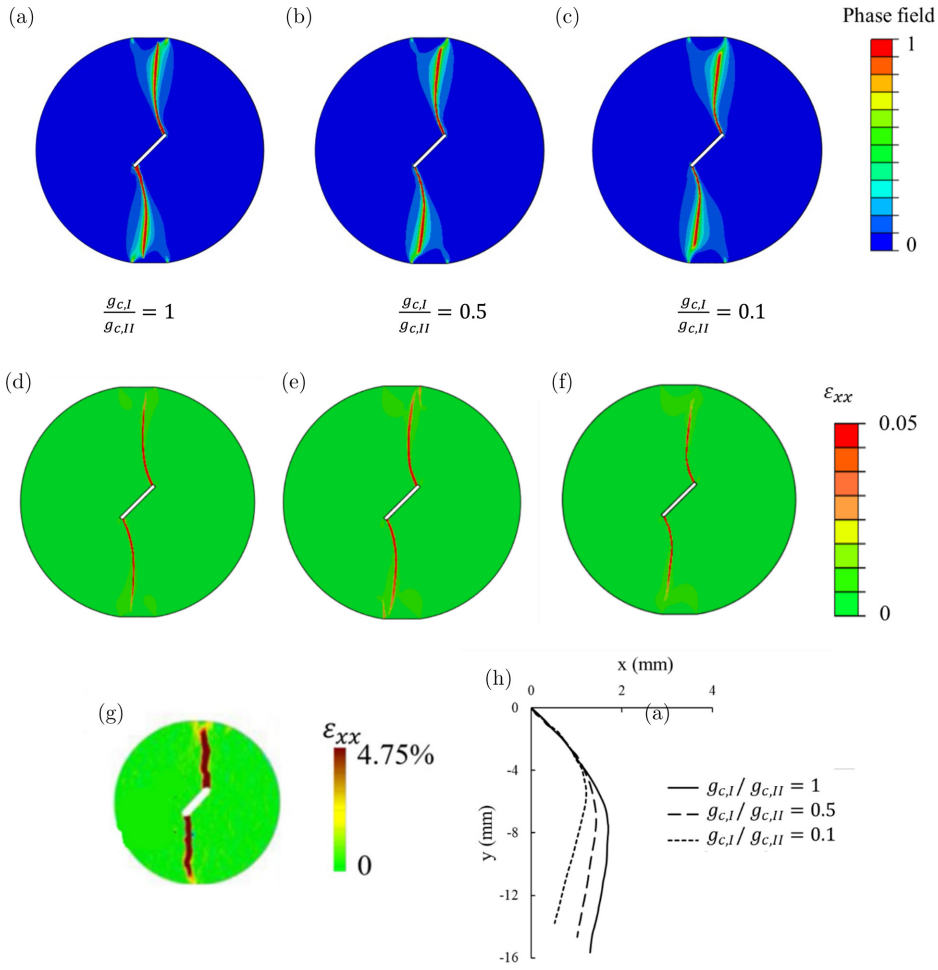

Fig. 6. The final crack patterns for the disc with a single 45° inclined flaw from (a)–(c) the phase-field contour from the modified model using different energy release rate ratios; (d) and (e) the ε_{xx} contour from modified model; (g) failure pattern represented by ε_{xx} contour measured in experiment [24]; (h) Crack paths extracted from (a)–(c).

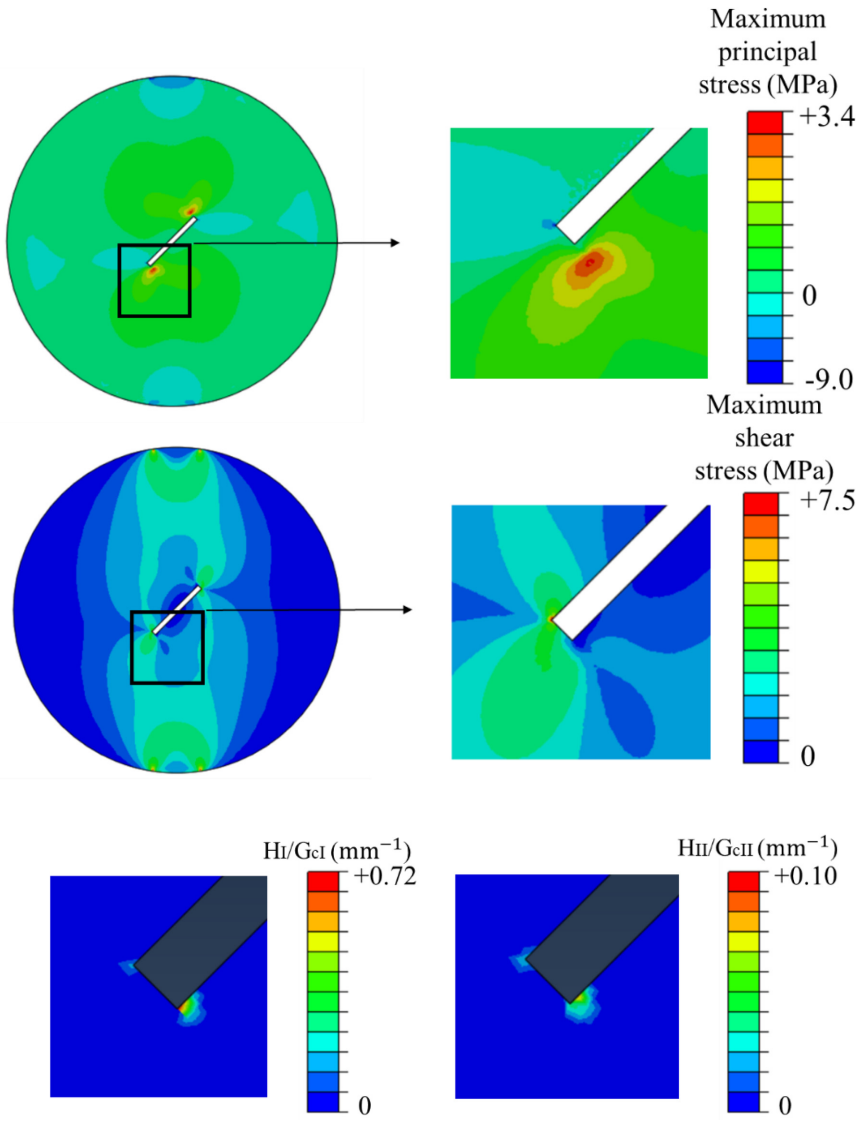

Fig. 7. Stress distribution and strain energy of the 45° single-flawed case at crack initiation with $\frac{g_{c.I}}{g_{c.II}} = 0.1$.

at the tip of the initiated crack, which drives the subsequent propagation. The maximum principal stress at the right-hand side of the tip of the bottom flaw is significantly larger than the maximum shear stress, which indicates that the tensile rather than the shear stress dominates the crack initiation. This is consistent with the experiment [24], where the crack initiation results from tension and the displacement vectors are along the flaw edge. The maximum shear stress concentrates on the left-hand side of the bottom tip, but the value is not large enough to initiate a crack before the propagation of the primary wing crack. In addition, the ratio $\frac{H}{g_c}$ dominates the critical state of the crack initiation. Based on the fracture mechanics theory, the energy release rate of the brittle material is determined as $g_c = \frac{K^2}{E}$, where g_c, K and E are energy release rate, toughness and Young's modulus, respectively [15]. Based on Eq. (3.13), a smaller value of g_{cI} means that the mode I toughness is also smaller, so that $\frac{H_1}{g_{cI}}$ increases faster. As shown in Fig. 7, $\frac{H_1}{g_{cI}}$ is nearly seven times larger than $\frac{H_2}{g_{cII}}$, which indicates that the ratio $\frac{H}{g_c}$ for mode I increases faster, and consequently the mode I fracture occurs first.

The test of the specimen with a vertical pre-existing flaw ($\alpha = 90°$) is also simulated using the modified model with $\frac{g_{c.I}}{g_{c.II}} = 0.1$. The progressive propagation results are shown in Fig. 8. As the potential crack paths are vertical, the width of the critical zone is set to be 6 mm with a total of 30,000 elements to reduce the computational cost in this case. The crack pattern is not influenced by adjusting the energy release rates. In this case, the two cracks initiate at both tips of the pre-existing flaw and propagate vertically until reaching the top and bottom surfaces.

In addition, the comparison of the stress–strain curves for these single-flawed discs with different inclination angles between the experimental and numerical results is illustrated in Fig. 9. The results from the simulation show a good agreement with the experimental ones. The critical values of displacement for both simulation cases are consistent with the corresponding experimental results. As for the post-crack zone, the simulated failure load of the pure tension test with vertical flaw matches well with the experiment. However, the load of the simulation with $\alpha = 45°$ drops considerably after the peak value, while the experimental curve keeps nearly flat. Note that

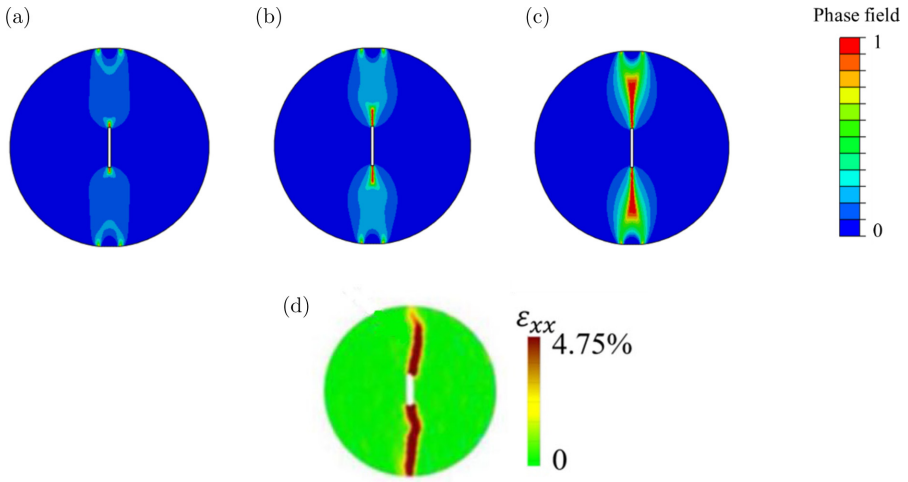

Fig. 8. Crack pattern for a Brazilian disc with a vertical single flaw at the displacement (a) $u = 0.65$ mm; (b) $u = 0.72$ mm; (c) $u = 0.75$ mm from the modified phase-field model with $\frac{g_{c,I}}{g_{c,II}} = 0.1$; (d) failure pattern represented by ε_{xx} contour measured in the experiment [24].

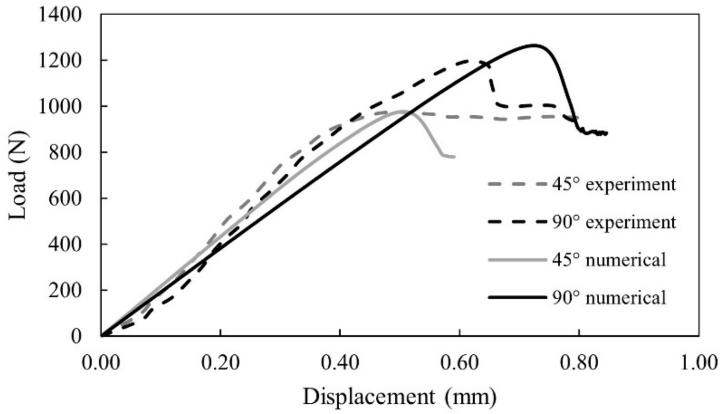

Fig. 9. Comparison of the load–displacement curves of the two specimens with a single central flaw between experimental results and numerical simulations.

the modification of the energy release rate may result in an overestimation of the load-carrying capacity. Overall, the model is capable of predicting the force-displacement response with the regulated value of the energy release rate.

5.2. Brazilian discs with two flaws

To further validate the capabilities of the modified phase-field model and explore the crack coalescence behavior, a series of double-flawed discs with various α (flaws angle) and β (bridge angle) under quasi-static compressive loading are simulated. The setup of the problem, including boundary conditions, mesh scenarios and load conditions, is the same as that for the single-flawed discs models above.

A specimen containing double flaws with $\alpha = 60°$, $\beta = 90°$ is modelled first to further investigate the effect of energy release rates on wing cracks. The crack patterns represented by the phase-field at crack initiation, inner crack coalescence and ultimate splitting in the modified and unmodified models are shown in Figs. 10(a)–10(c) and 10(d)–10(f), respectively. In both models, four wing cracks initiate at all tips of the double-flaws. The two outer cracks propagate towards the top and bottom of the disc. However, the effect of the modification on the coalescence of the inner cracks is significant in this case. In the modified model, two inner cracks link to each other at the centre of the disc. On the other hand, the occurrence of the coalescence in the unmodified model is different, where the two inner cracks propagate until connecting their opposite flaws tips. The ε_{xx} contour at failure stage from both the unmodified and modified model is shown in Figs. 10(g) and 10(h). The crack pattern, especially the coalescence of the inner cracks, from the modified model can reproduce the real crack paths, as shown in Fig. 10(i).

For verifying the modified model's capability of capturing the secondary cracks, the specimen with two colinear pre-existing flaws with $\alpha = 45°$, $\beta = 45°$ is also simulated. The progress of crack evolution is shown in Fig. 11. Again, all the four wing cracks initiate at the flaw tips. However, the propagation of the two inner wing cracks tends to be slower, and a shear zone emerges in the bridge zone, which connects the inner tips of two pre-existing flaws. Then, the secondary shear cracks are observed in the shear zone, which results in coalescence. Notably, the propagation of the shear cracks is very unstable, and the two pre-flaws coalesce with a very small displacement increment since the shear zone first emerges. The simulated crack patterns are consistent with the experimental results.

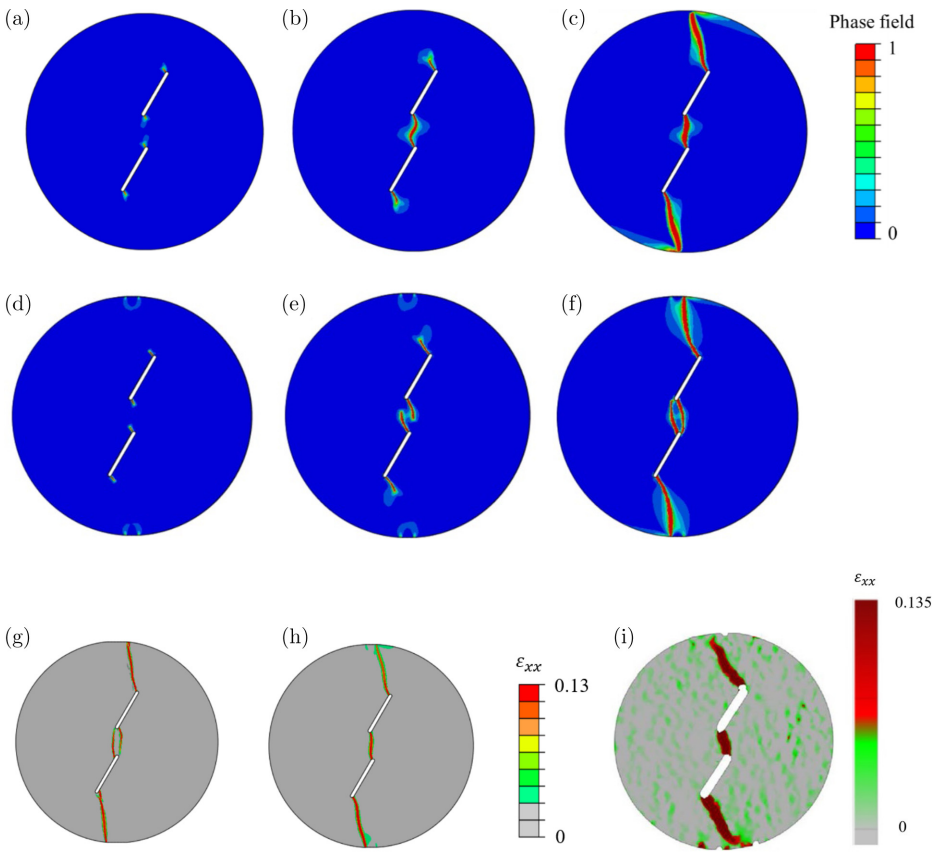

Fig. 10. Crack evolutions for the specimen with $\alpha = 60°$, $\beta = 90°$ from (a)–(c) modified phase-field model with $\frac{g_{c,I}}{g_{c,II}} = 0.1$; (d)–(f) unmodified phase-field model; (g) and (h) ε_{xx} contour at failure from unmodified and modified phase-field model; (i) contour of ε_{xx} measured by DIC in experiment [24].

Finally, the specimens containing overlapped double flaws with $\alpha = 45°$ & $\beta = 210°$ are also considered for studying more complex fracture behaviors. As can be seen from Fig. 12, the crack initiates at both tips of the two flaws. The two outer cracks propagate firstly, and their behaviors are similar to those in the single-flawed case with $\alpha = 45°$. The two outer cracks are initially almost perpendicular to the pre-existing flaws, which are deemed to be in mixed mode, and the initiation is dominated by shear. The orientation of the outer

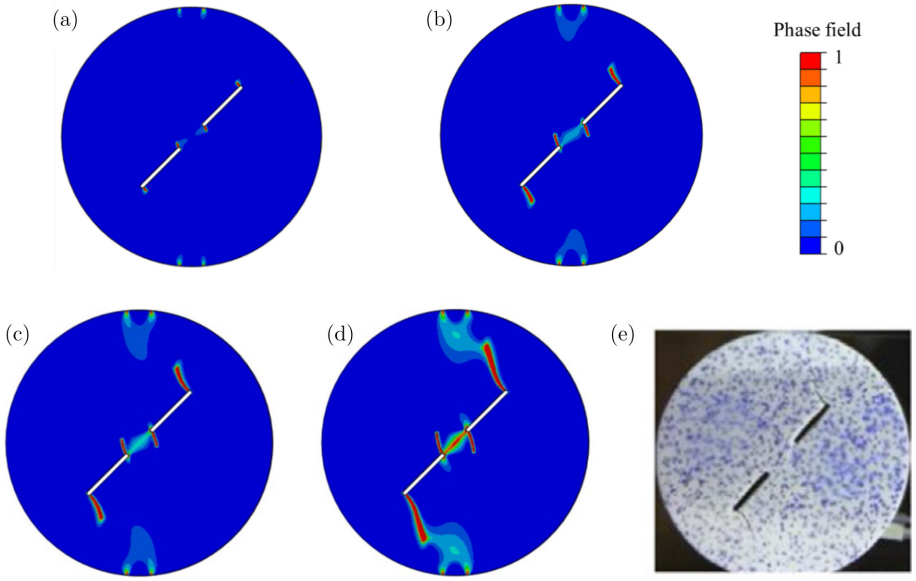

Fig. 11. Crack evolution for a double-flawed Brazilian disc with $\alpha = 45°$, $\beta = 45°$ for the displacement at (a) = 0.36 mm; (b) $u = 0.43$ mm; (c) $u = 0.52$ mm; (d) $u = 0.54$ mm; (e) crack image from the experiment [24].

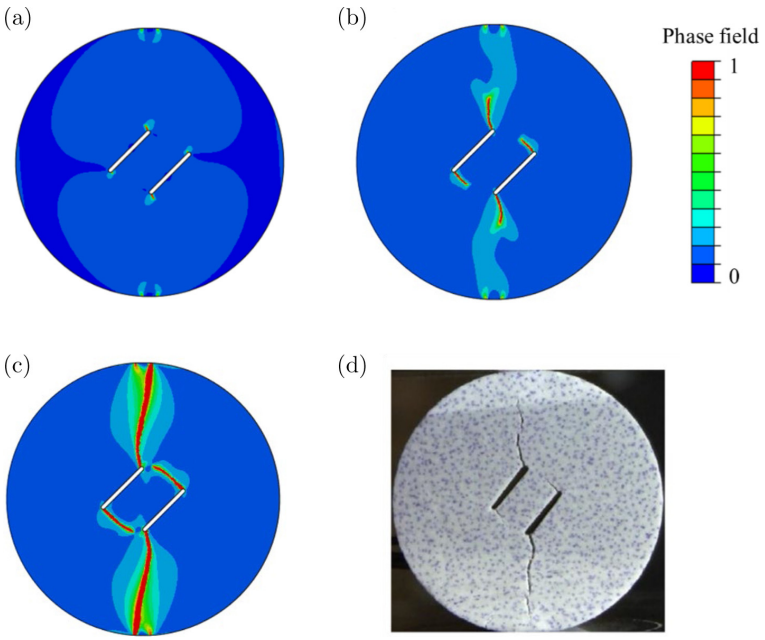

Fig. 12. Crack evolution for the double-flawed disc with $\alpha = 45°$ & $\beta = 210°$ at a displacement of (a) $= 0.62$ mm; (b) $u = 0.84$ mm; (c) $u = 1$ mm from the modified phase-field model; (d) crack image from the experiment [24].

crack propagation quickly becomes vertical as the cracks are dominated by tensile strain, and finally, the cracks penetrate the top and bottom surfaces of the disc. On the other hand, significant propagation of the two inner cracks is observed right after the start of the development of the outer cracks. The inner cracks develop along the line nearly perpendicular to the pre-existing flaws until the inner area is fully split. The observations of the crack paths from the simulation and the experiment are consistent. The ultimate crack pattern and sequence of the evolution of the outer and inner cracks are reasonably reproduced. The evolution of the horizontal normal strain ε_{xx} and the real surface crack pattern from the experiment are also shown in Fig. 13. The length of the inner cracks observed in the experimental data is shorter than that from the simulation. The reason is deemed to be that the displacement of two sides of the crack opening around the crack tip is too small to be observed even if it is fully cracked with $\varphi = 1$. To better compare the results, the evolution of horizontal normal strain contour at crack initiation and failure from both the simulation and the experiment is shown in Fig. 13. As observed, the horizontal normal strain is consistent with the experimental results.

In addition, the comparison of the crack initiation load (peak load) and coalescence load between the numerical results and the

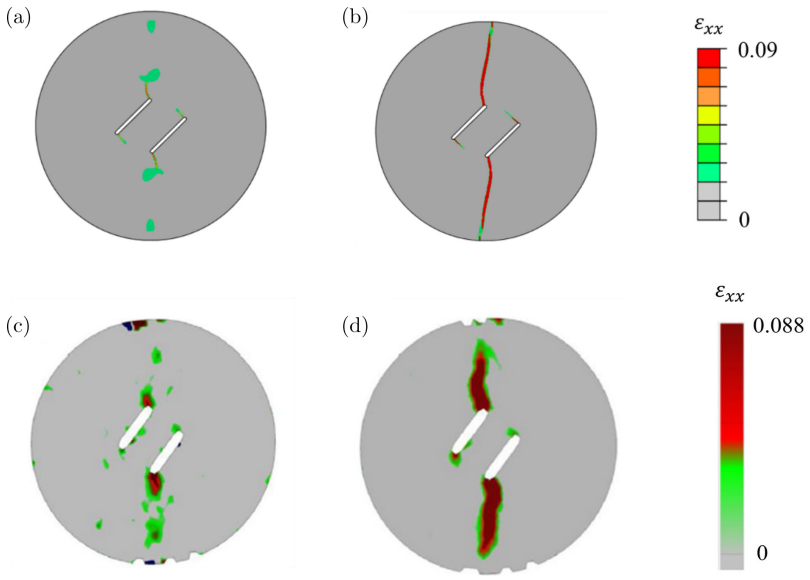

Fig. 13. Comparison between the evolution of horizontal normal strain ε_{xx} contour for the double-flawed disc with $\alpha = 45°$ & $\beta = 210°$ obtained from (a) and (b) the phase-field model with $\frac{g_{c,I}}{g_{c,II}} = 0.1$ and (c) and (d) the experiment [24].

Table 1. Comparison of the peak load and the coalescence load of double-flawed tests between experimental results and simulations.

Flaws orientation	Peak load from experiments (N)	Peak load from simulations (N)	Coalescence load from experiments (N)	Coalescence load from simulations (N)	Coalescence type
$\alpha = 60°$, $\beta = 90°$	1360	1201	1110	1026	Tensile
$\alpha = 45°$, $\beta = 45°$	904	977	860	957	Shear
$\alpha = 45°$, $\beta = 210°$	1413	1317	1182	1018	Tensile

experimental data is shown in Table 1. The simulation results are in good agreement with the experiment, and the differences among all three cases are around 10%. Also, the coalescence types of these three cases from the simulation are consistent with those from the experiment. The simulated loads from the case with $\alpha = 45°$ & $\beta = 45°$ are larger than the experimental ones, while those from the other two cases are smaller. This is believed to result from changing the energy release rate to $\frac{g_{c,I}}{g_{c,II}} = 0.1$. With a small value of $\frac{g_{c,I}}{g_{c,II}}$, the shear crack occurs with a higher value of stress and strain as the mode II fracture toughness increases accordingly.

6. Conclusion

In this study, a phase-field method for quasi-static brittle fracture is proposed and further modified by considering the distinction of critical energy release rates for mode I and II cracks. The model is implemented in ABAQUS with a user-defined subroutine and is used to simulate the complex crack initiation, propagation, branching and coalescence in several rock-like 3D printed Brazilian discs with single or double flaws under quasi-static compression. The simulation results are in good agreement with the experimental observations both qualitatively and quantitively.

The impact of modified energy release rates on wing cracks is captured and analyzed in the case with 45° single flaw. The crack propagation is dominated by tensile stress with a smaller $g_{c,I}$, consistent with the experiments. The double-flawed case with $\alpha = 60°$ & $\beta = 90°$ further investigates the effect of decreasing $g_{c,I}$ on wing cracks. In particular, the coalescence of inner cracks in the rock bridge zone differs significantly between the modified and unmodified models. The capability of the modified model for capturing the secondary shear crack is verified by the case with $\alpha = 45°$ & $\beta = 45°$ in which the shear crack at the disc centre reproduces the experimental result. Furthermore, the crack initiation and propagation of the disc with overlapped double flaws are captured in the last case. It is observed that a decrease in the ratio $\frac{g_{c,I}}{g_{c,II}}$ reduces the mode I toughness, which impacts the mixed-mode crack propagation and coalescence. For the cases with inclined pre-existing flaws, the effect is significant on the primary wing cracks. Hence, it is necessary to consider the energy release rates for modes I and II separately to capture their effects on the cracking behavior of rock-like materials.

Despite of excellent performance of the proposed modified phase-field model, it is worth noting that the current approach may have certain limitations. The splitting of different energy release rates for modes I and II is a relatively simplified method without determining the direction of crack propagation which maximizes energy dissipation. Even though the crack initiation, propagation and/or coalescence of single-flawed and double-flawed cases can be successfully predicted, it may be still hard to predict the complex mixed-mode fractures such as branching in some complicated cases. In summary, this study demonstrates the significance of the energy release rate ratio in the phase-field model for simulating the fracture behaviors of rock-like materials, as well as the applicability and capability of the proposed model in capturing complex brittle cracks.

Acknowledgments

This work was supported in part by the Australian Research Council through Discovery Projects Scheme (Grant Nos. DP190102954 and DP200101919). The authors acknowledge the use of the National Computational Infrastructure (NCI) which is supported by the Australian Government, and accessed through the Sydney Informatics Hub HPC Allocation Scheme, which is supported by the Deputy Vice-Chancellor (Research), University of Sydney.

References

[1] E. Karatela, A. Taheri, C. Xu and G. Stevenson. Study on effect of *in-situ* stress ratio and discontinuities orientation on borehole stability in heavily fractured rocks using discrete element method. *Journal of Petroleum Science & Engineering* **139**, pp. 94–103, 2016.

[2] J. H. Song and T. Belytschko. Cracking node method for dynamic fracture with finite elements. *International Journal for Numerical Methods in Engineering* **77**(3), pp. 360–385, 2009.

[3] J. J. Marigo, C. Maurini and K. Pham. An overview of the modelling of fracture by gradient damage models. *Meccanica (Milan)* **51**(12), pp. 3107–3128, 2016.

[4] M. Ambati, T. Gerasimov and L. de Lorenzis. A review on phase-field models of brittle fracture and a new fast hybrid formulation. *Computational Mechanics* **55**(2), pp. 383–405, 2014.

[5] M. R. Carvalho, J. A. Barros, Y. Zhang and D. Dias-da-Costa. A computational model for simulation of steel fibre reinforced concrete with explicit fibres and cracks. *Computer Methods in Applied Mechanics and Engineering* **363**, p. 112879, 2020.

[6] D. Dias-da-Costa, J. Alfaiate, L. J. Sluys and E. Júlio. A discrete strong discontinuity approach, *Engineering Fracture Mechanics* **76**(9), pp. 1176–1201, 2009.

[7] T. P. Fries and T. Belytschko. The extended/generalized finite element method: an overview of the method and its applications. *International Journal for Numerical Methods in Engineering* **84**(3), pp. 253–304, 2010.

[8] P. O. Bouchard, F. Bay, Y. Chastel and I. Tovena. Crack propagation modelling using an advanced remeshing technique. *Computer Methods in Applied Mechanics and Engineering* **189**(3), pp. 723–742, 2000.

[9] R. de Borst, J. J. C. Remmers, A. Needleman and M.-A. Abellan. Discrete vs smeared crack models for concrete fracture: Bridging the gap. *International Journal for Numerical and Analytical Methods in Geomechanics* **28**(7–8), pp. 583–607, 2004.

[10] C. Miehe, F. Welschinger and M. Hofacker. Thermodynamically consistent phase-field models of fracture: Variational principles and multi-field FE implementations. *International Journal for Numerical Methods in Engineering* **83**(10), pp. 1273–1311, 2010a.

[11] C. Miehe, M. Hofacker and F. Welschinger. A phase field model for rate-independent crack propagation: Robust algorithmic implementation based on operator splits. *Computer Methods in Applied Mechanics and Engineering* **199**(45), pp. 2765–2778, 2010b.

[12] B. Bourdin, G. A. Francfort and J.-J. Marigo. The variational approach to fracture. *Journal of Elasticity* **91**(1), pp. 5–148, 2008.

[13] G. A. Francfort and J.-J. Marigo. Revisiting brittle fracture as an energy minimization problem. *Journal of the Mechanics and Physics of Solids* **46**(8), pp. 1319–1342, 1998.

[14] A. A. Griffith. The phenomena of rupture and flow in solids. *Philosophical Transactions of the Royal Society of London. Series A* **221**, pp. 163–198, 1921.

[15] G. R. Irwin. Analysis of stresses and strains near the end of a crack traversing a plate. *Journal of Applied Mechanics* **24**, pp. 361–364, 1957.

[16] R. de Borst and C. V. Verhoosel. Gradient damage vs phase-field approaches for fracture: Similarities and differences. *Computer Methods in Applied Mechanics and Engineering* **312**, pp. 78–94, 2016.
[17] M. Hofacker and C. Miehe. A phasefield model of dynamic fracture: Robust field updates for the analysis of complex crack patterns. *International Journal for Numerical Methods in Engineering* **93**(3), pp. 276–301, 2013.
[18] C. Li, J. Fang, C. Wu, G. Sun, G. Steven and Q. Li. (2022). Phase field fracture in elasto-plastic solids: Incorporating phenomenological failure criteria for ductile materials. *Computer Methods in Applied Mechanics and Engineering* **391**, p. 114580, 2022.
[19] C. Miehe and S. Mauthe. Phase field modeling of fracture in multi-physics problems. Part III. Crack driving forces in hydro-poro-elasticity and hydraulic fracturing of fluid-saturated porous media. *Computer Methods in Applied Mechanics and Engineering* **304**, pp. 619–655, 2016.
[20] S. Zhou, X. Zhuang, J. Zhou and F. Liu. Phase field characterization of rock fractures in Brazilian splitting test specimens containing voids and inclusions. *International Journal of Geomechanics* **21**(3), p. 04021006, 2021.
[21] U. Pillai, S. P. Triantafyllou, Y. Essa and F. M. de la Escalera, An anisotropic cohesive phase field model for quasi-brittle fractures in thin fibre-reinforced composites. *Composite Structures* **252**, p. 112635, 2020.
[22] C. Wu, J. Fang, Z. Zhang, A. Entezari, G. Sun, M. V. Swain and Q. Li, Fracture modeling of brittle biomaterials by the phase-field method. *Engineering Fracture Mechanics* **224**, p. 106752, 2020.
[23] R. A. Stirling, D. J. Simpson and C. T. Davic. The application of digital image correlation to Brazilian testing of sandstone. *International Journal of Rock Mechanics and Mining Sciences* **60**, pp. 1–11, 2013.
[24] M. Sharafisafa, L. Shen and Q. Xu. Characterisation of mechanical behaviour of 3D-printed rock-like material with digital image correlation. *International Journal of Rock Mechanics and Mining Sciences* **112**, pp. 122–138, 2018.
[25] M. Sharafisafa, L. Shen, Y. Zheng and J. Xiao. The effect of flaw filling material on the compressive behaviour of 3D printed rock-like discs. *International Journal of Rock Mechanics and Mining Sciences* **117** pp. 105–117, 2019.
[26] M. Sharafisafa, Z. Aliabadian and L. Shen. Crack initiation and failure of block-in-matrix rocks under Brazilian test using digital image correlation. *Theoretical and Applied Fracture Mechanics* **109**, p. 102743, 2020.
[27] L. Yang, M. Sharafisafa and L. Shen. On the fracture mechanism of rock-like materials with interbedded hard-soft layers under Brazilian tests. *Theoretical and Applied Fracture Mechanics* **116**, p. 103102, 2021.
[28] S. Zhou and C. Xia. Propagation and coalescence of quasi-static cracks in Brazilian disks: An insight from a phase field model. *Acta Geotechnica* **14**(4), pp. 1195–1214, 2018.
[29] C. Bilgen, S. Homberger and K. Weinberg. Phase-field fracture simulations of the Brazilian splitting test. *International Journal of Fracture* **220**(1), pp. 85–98, 2019.
[30] X. Zhou, L. Wang and Y. Shou. Understanding the fracture mechanism of ring Brazilian disc specimens by the phase field method. *International Journal of Fracture* **226**(1), pp. 17–43, 2020.
[31] X. Zhang, S. W. Sloan, C. Vignes and D. Sheng. A modification of the phase-field model for mixed mode crack propagation in rock-like materials. *Computer Methods in Applied Mechanics and Engineering* **322**, pp. 123–136, 2017.
[32] M. Nejati, B. Bahrami, M. R. Ayatollahi and T. Driesner. On the anisotropy of shear fracture toughness in rocks. *Theoretical and Applied Fracture Mechanics* **113**, p. 102946, 2021.
[33] X. Zhou and Y. Wang. Numerical simulation of crack propagation and co-alescence in pre-cracked rock-like Brazilian disks using the non-ordinary state-based peridynamics. *International Journal of Rock Mechanics and Mining Sciences* **89**, pp. 235–249, 2016.
[34] G. Molnár and A. Gravouil. 2D and 3D ABAQUS implementation of a robust staggered phase-field solution for modeling brittle fracture. *Finite Elements in Analysis and Design* **130**, pp. 27–38, 2017.
[35] M. Asadi-Eydivand, M. Solati-Hashjin and N. A. Abu Osman. Mechanical behavior of calcium sulfate scaffold prototypes built by solid free-form fabrication. *Rapid Prototyping Journal* **24**(8), pp. 1392–1400, 2018.
[36] R. Hamano, Y. Nakagawa, V. Irawan and T. Ikoma, Mechanical anisotropy and fracture mode of binder jetting 3D printed calcium sulfate moldings. *Applied Materials Today* **25**, p. 101160, 2021.
[37] D. Li and L. N. Y. Wong. The Brazilian disc test for rock mechanics applications: Review and new insights. *Rock Mechanics and Rock Engineering* **46**(2), pp. 269–287, 2012.
[38] P. K. Kristensen and M. P. Emilio. Phase field fracture modelling using quasi-Newton methods and a new adaptive step scheme. *Theoretical and Applied Fracture Mechanics* **107**, p. 102446, 2020.
[39] M. Entacher, E. Schuller and R. Galler. Rock failure and crack propagation beneath disc cutters. *Rock Mechanics and Rock Engineering* **48**(4), pp. 1559–1572, 2015.
[40] E. C. Bryant and W. Sun. A mixed-mode phase field fracture model in anisotropic rocks with consistent kinematics. *Computer Methods in Applied Mechanics and Engineering*, **342**(C), pp. 561–584, 2018.
[41] Q. Wang, Y. Feng, W. Zhou, Y. Cheng and G. Ma. A phase-field model for mixed-mode fracture based on a unified tensile fracture criterion. *Computer Methods in Applied Mechanics and Engineering*, **370**, p. 113270, 2020.
[42] ABAQUS, ABAQUS Documentation, Dassault Systemes, Providence, RI, USA, 2011.
[43] J. J. Remmers, R. de Borst and A. Needleman. The simulation of dynamic crack propagation using the cohesive segments method. *Journal of the Mechanics and Physics of Solids*, **56**(1), pp. 70–92, 2008.